



Thermal Stability of Milled Nanocrystalline Tungsten Powders

by Brady Butler, Eric Klier, Matt Kelly, and Micah Gallagher

ARL-TR-5541

May 2011

NOTICES

Disclaimers

The findings in this report are not to be construed as an official Department of the Army position unless so designated by other authorized documents.

Citation of manufacturer's or trade names does not constitute an official endorsement or approval of the use thereof.

Destroy this report when it is no longer needed. Do not return it to the originator.

Army Research Laboratory

Aberdeen Proving Ground, MD 21005

ARL-TR-5541**May 2011**

Thermal Stability of Milled Nanocrystalline Tungsten Powders

**Brady Butler, Eric Klier, Matt Kelly, and Micah Gallagher
Weapons and Materials Research Directorate, ARL**

REPORT DOCUMENTATION PAGE			Form Approved OMB No. 0704-0188		
<p>Public reporting burden for this collection of information is estimated to average 1 hour per response, including the time for reviewing instructions, searching existing data sources, gathering and maintaining the data needed, and completing and reviewing the collection information. Send comments regarding this burden estimate or any other aspect of this collection of information, including suggestions for reducing the burden, to Department of Defense, Washington Headquarters Services, Directorate for Information Operations and Reports (0704-0188), 1215 Jefferson Davis Highway, Suite 1204, Arlington, VA 22202-4302. Respondents should be aware that notwithstanding any other provision of law, no person shall be subject to any penalty for failing to comply with a collection of information if it does not display a currently valid OMB control number.</p> <p>PLEASE DO NOT RETURN YOUR FORM TO THE ABOVE ADDRESS.</p>					
1. REPORT DATE (DD-MM-YYYY) May 2011		2. REPORT TYPE Interim		3. DATES COVERED (From - To) 1 January 2009 to 31 December 2010	
4. TITLE AND SUBTITLE Thermal Stability of Milled Nanocrystalline Tungsten Powders			5a. CONTRACT NUMBER		
			5b. GRANT NUMBER		
			5c. PROGRAM ELEMENT NUMBER		
6. AUTHOR(S) Brady Butler, Eric Klier, Matt Kelly, and Micah Gallagher			5d. PROJECT NUMBER		
			5e. TASK NUMBER		
			5f. WORK UNIT NUMBER		
7. PERFORMING ORGANIZATION NAME(S) AND ADDRESS(ES) U.S. Army Research Laboratory ATTN: RDRL-WMM-F Aberdeen Proving Ground, MD 21005			8. PERFORMING ORGANIZATION REPORT NUMBER ARL-TR-5541		
9. SPONSORING/MONITORING AGENCY NAME(S) AND ADDRESS(ES)			10. SPONSOR/MONITOR'S ACRONYM(S)		
			11. SPONSOR/MONITOR'S REPORT NUMBER(S)		
12. DISTRIBUTION/AVAILABILITY STATEMENT Approved for public release; distribution unlimited.					
13. SUPPLEMENTARY NOTES					
14. ABSTRACT <p>The development of nanocrystalline and ultrafine-grained bulk materials through powder metallurgy processes has long been constrained by the thermal stability of nanostructures. Many difficulties arise due to the fact that grain growth and densification occur within the same temperature regime. Additionally, the mechanisms supporting densification require some degree of grain coarsening in order to achieve full density. This study outlines the development of a thermally stable nanocrystalline tungsten powder and discusses the influence of grain size stability on the overall densification rate during pressureless sintering in hydrogen atmosphere. Furthermore, the activation energy of sintering is calculated to determine whether the mechanisms of grain growth and densification can be decoupled through the addition of thermal grain stabilizers.</p>					
15. SUBJECT TERMS Tungsten, nano, thermal stability					
16. SECURITY CLASSIFICATION OF:			17. LIMITATION OF ABSTRACT UU	18. NUMBER OF PAGES 24	19a. NAME OF RESPONSIBLE PERSON Brady Butler
a. REPORT Unclassified	b. ABSTRACT Unclassified	c. THIS PAGE Unclassified			19b. TELEPHONE NUMBER (Include area code) (410) 306-0835

Contents

List of Figures	iv
List of Tables	iv
Acknowledgments	v
1. Introduction	1
2. Experimental Procedure	2
2.1 Master Sintering Curve Calculations	2
2.2 Determining the Apparent Activation Energy for Densification	4
3. Results and Discussion	5
4. Summary and Conclusions	11
5. References	12
List of Symbols, Abbreviations, and Acronyms	14
Distribution List	15

List of Figures

Figure 1. Arrhenius plot for the determination of the apparent activation energy of densification.....	5
Figure 2. Grain size measurements acquired by x-ray diffraction for each of the thermally stabilized nano-tungsten powders.....	6
Figure 3. Electron micrographs, grain sizes and densities of three tungsten samples processed under different milling conditions.....	7
Figure 4. Densification behavior of milled nanostructured tungsten powders.....	7
Figure 5. Apparent activation energy for densification of milled tungsten powders exhibiting different degrees of microstructural stability. Note that the differences in initial density are a result of different green packing densities resulting from dissimilar milling conditions.....	8
Figure 6. Plot of the measured apparent activation energy as a function of grain pinner concentration and grain size.....	9
Figure 7. Master sintering curves for tungsten powders under different milling conditions. Each master sintering curve represents the dilatometry results from three different heating rates (3, 10, and 25 °C/min.).....	10

List of Tables

Table 1. Measured activation energies for self diffusion based on three mass-transport mechanisms in pure tungsten (20, 28).	9
--	---

Acknowledgments

This research is supported by mission funding from the Depleted Uranium Replacement Program and is the result of collaborative efforts from a number of team members. Special thanks are given to Bradley Klotz for excellent work on the microstructural characterization of these materials.

INTENTIONALLY LEFT BLANK.

1. Introduction

This report presents factors identified that influence the thermal stability and sinterability of nanocrystalline tungsten. In addition to conventional methods of determining the stability of ultrafine and nanocrystalline grain structures, these tungsten materials were analyzed using a novel in-situ dilatometry technique, which identifies the thermal stability and densification behavior concurrently. This was accomplished by identifying the activation energy for densification and developing master sintering curves.

Nanocrystalline materials have long held the promise of demonstrating improved performance over their microcrystalline counterparts. While recent years have seen much advancement in producing bulk nanocrystalline materials through various novel processing techniques (1–3), the commercial application of these materials requires a significant reduction in processing costs to be viable in all but a few niche markets. In particular, bottom-up powder processing and consolidation techniques have shown promise for developing a cost-effective method for creating bulk nanocrystalline materials. While significant research has been performed in consolidating nanocrystalline powders (4–6), there remains some difficulty in achieving full density while retaining the nanostructure of the milled powders. Unstable nanostructures have significantly higher atomic mobility than their coarse-grained counterparts. This increased mobility tends to reduce the temperature required to sinter to a desired density; however, this mobility also causes rapid grain growth to occur during the densification.

Nanocrystalline materials have a very large volume fraction of grain boundary area, making these materials inherently unstable as a result of incomplete bonding at the interface between grains. Within the past decade, there has been significant research to improve the thermal stability of nanostructures by limiting the propensity of grain growth through kinetic inhibitors (7, 8) or thermodynamic stabilizers (9–11). The most commonly used method for improving stability is a kinetic method termed Zener pinning, where the mobility of the grain boundaries is impeded by the addition of small insoluble particles that sit preferentially at the grain boundary interface and must be dragged along the path of the growing grain. While the methods and mechanisms for increasing thermal stability have been described in some detail (12), proper analysis of this stability requires a thorough inspection of the rate dependence for grain growth. This is often achieved through Kissinger analysis of calorimetry curves (13) or by analysis of the grain size at different stages in the sintering process using x-ray diffraction (14, 15) or electron microscopy (16) of specimens annealed to different temperatures. These techniques tend to be very time consuming and most researchers are content to describe the thermal stability of a material by referring to the grain size after sintering (17–19).

While thermal stability is critical for retaining the nanostructure of the as-prepared powders, the densification behavior is equally important to the final properties of a sintered material. In many cases, increasing the thermal stability of a material can drastically reduce the ability to achieve full density by inhibiting the diffusion required for densification. Although densification factors are very important for identifying sintering guidelines and achieving a quality final product, it is often presented independently from the thermal stability of grains.

2. Experimental Procedure

Three tungsten powders labeled High Stability (HS), Moderate Stability (MS), and Low Stability (LS) were prepared by milling tungsten powder in a high energy mill. Milling parameters were selected so that essentially pure tungsten powders were prepared with various levels of grain pinning impurities leading to varying degrees of thermal stability in each sample. Powder samples were analyzed in a Panalytical X'Pert PRO Materials Research Diffractometer (MRD) to determine particle size and lattice strain. Direct current plasma emission spectroscopy was used to identify the concentration of trace grain pinning elements in each sample.

Milled tungsten samples were compacted using a cold isostatic press and sintered in a 99.999% hydrogen atmosphere using a Thermal Technologies furnace or a Netzsch 402E Dilatometer. Each sample was reduced for 3 h at 700 °C in order to remove surface oxidation that can inhibit densification while increasing the propensity for grain growth (20). Dilatometry data were collected at three constant heating rates: 3, 10, and 25 °C/min. The data from these measurements were used to determine the apparent activation energy for sintering and develop master sintering curves. The final density of the sintered samples was tested using the Archimedes method. Grain size was analyzed using x-ray diffraction (XRD), scanning electron microscopy (SEM), and transmission electron microscopy (TEM).

2.1 Master Sintering Curve Calculations

Classical sintering theory distinguishes three different stages in the sintering process based upon the dominant sintering mechanism and diffusion processes that are occurring in the sample (21). Stage one begins at low temperatures where surface diffusion connects particles and creates regions of necking with minimal increases in density. Stage two shows the greatest increase in density and has grain boundary diffusion and possibly volume diffusion as the predominant mass transport mechanisms. The removal of small pores and coarsening of grains are characteristic of the third stage of sintering where volume diffusion tends to dominate.

Many sintering theories have been developed to describe the densification behavior of a material based on the diffusion mechanisms that lead to densification in the sample. A combined stage sintering model developed by Su and Johnson (22) shows the linear shrinkage rate as a function of the microstructural and diffusion properties of a material:

$$-\frac{dL}{Ldt} = \frac{\gamma\Omega}{kT} \left(\frac{\Gamma_v D_v}{G^3} + \frac{\Gamma_b \delta D_b}{G^4} \right). \quad (1)$$

This equation relates the normalized instantaneous shrinkage rate of the specimen $\left(\frac{dL}{Ldt} \right)$ to the surface tension (γ), grain size (G), and the coefficients for volume and grain boundary diffusion (D_v and D_b , respectively) at each of the three stages of the sintering process, where Ω is the atomic volume; k is Boltzmann's constant; T is the absolute temperature; Γ_v and Γ_b are constants for scaling the microstructure of volume and grain boundary diffusion, respectively; and δ is the grain boundary thickness. The surface diffusion term is generally neglected because it does not generally contribute to the densification process, though it can be responsible for significant coarsening in the specimen. Equation 1 can be further modified to represent the instantaneous density by substituting the following relation, which is valid for isotropic shrinkage during densification:

$$-\frac{dL}{Ldt} = \frac{d\rho}{3\rho dt}, \quad (2)$$

where ρ is the instantaneous density of the specimen. If there is only one dominant diffusion mechanism contributing to the densification process, the diffusion terms can be simplified and expanded as shown in equation 3:

$$\left(\frac{\Gamma_v D_v}{G^3} + \frac{\Gamma_b \delta D_b}{G^4} \right) = \frac{[\Gamma(\rho)]D_0}{[G(\rho)]^n} \exp\left(-\frac{Q}{RT}\right), \quad (3)$$

where R is the universal gas constant, Q is the apparent activation energy, and n is 3 or 4 depending on whether the process is volume or grain boundary diffusion controlled. Combining equations 1 and 2 and substituting the result from equation 3 leads to

$$\frac{d\rho}{3\rho dt} = \frac{\gamma\Omega[\Gamma(\rho)]D_0}{kT[G(\rho)]^n} \exp\left(-\frac{Q}{RT}\right). \quad (4)$$

In equation 4, the terms that describe microstructural evolution of the material as a function of density can be separated from the diffusion terms, which are dependent on the time and temperature profile of the processing as shown by equation 5:

$$\int_{\rho_0}^{\rho} \frac{[G(\rho)]^n}{3\rho\Gamma(\rho)} d\rho = \int_0^t \frac{\gamma\Omega D_0}{kT} \exp\left(-\frac{Q}{RT}\right) dt. \quad (5)$$

The integration of equation 5 requires the microstructural characteristics of the specimen be independent of the time-temperature profile of the system and solely a function of the total density of the specimen. While this assumption is not adequate for complex sintering processes (23), it is justifiable for certain constant heating rate experiments and has been proven accurate

for both metal (24, 25) and ceramic (22, 26, 27) systems in general. Equation 5 can be rearranged to separate the functions for density and time/temperature dependence; the results are shown as equations 6 and 7, respectively.

$$\Phi(\rho) = \frac{k}{\gamma\Omega D_0} \int_{\rho_0}^{\rho} \frac{[G(\rho)]^n}{3\rho\Gamma(\rho)} d\rho \quad (6)$$

$$\Theta(t, T) = \int_0^t \frac{1}{T} \exp\left(-\frac{Q}{RT}\right) dt \quad (7)$$

In equation 7, $\Theta(t, T)$ can be described as the total amount of thermal work that is put into the system, while $\Phi(\rho)$ describes the resulting density, grain size, and microstructural characteristics of the system. The foundation of the master sintering curve is shown in the relationship between these parameters as described by equation 8:

$$\Phi(\rho) = \Theta(t, T). \quad (8)$$

For any given energy input described by $\Theta(t, T)$, there will be a resulting density, grain size, and microstructural parameter as described by $\Phi(\rho)$.

2.2 Determining the Apparent Activation Energy for Densification

The activation energy of the system can be estimated from constant heating rate experiments if Γ and G are independent of the heating rate. Furthermore, if there is only one dominant diffusion mechanism active during the measured portion of the sintering cycle, the activation energy will be close to the tabulated value for the activation energy of diffusion. Conversely, the changes in the grain size or microstructural properties that result from different heating rates will become apparent in the activation energy term. Γ and G are never entirely independent of thermal processing conditions and the activation energy measured in these experiments is referred to as the “apparent activation energy for densification” to mark this distinction. In certain systems, specifically unstable nanocrystalline powders, the grain size and microstructural terms clearly change when sintering; however, thermally stable nanostructures are inherently less dependent on temperature and these terms can be considered to remain constant.

The apparent activation energy for densification can be determined from dilatometry curves by using an Arrhenius plot for constant heating rate of $\ln\left(\frac{d\rho}{dt} * \dot{T} * T\right)$ VS $\frac{1}{T}$, where \dot{T} is the

heating rate, T is the absolute temperature, and $\frac{d\rho}{dt}$ is the instantaneous densification rate. The slope of the fitted lines at each density is equal to the activation energy divided by the negative of the universal gas constant as shown in figure 1.

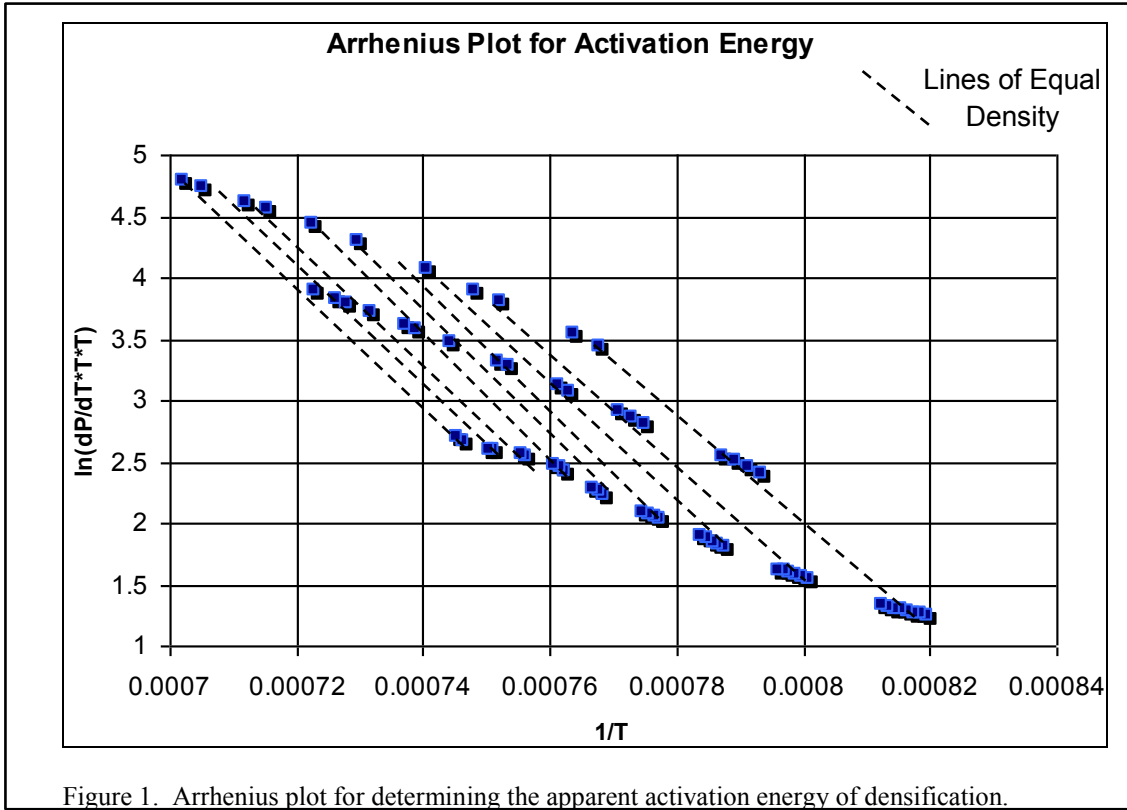


Figure 1. Arrhenius plot for determining the apparent activation energy of densification.

The activation energy was measured using this method so that the variation in activation energy could be measured as a function of density in order to identify the mechanisms operating at different stages of the sintering process. Other methods commonly use a least squares fit of the master sintering curve to describe the average activation energy. While the activation energy does vary as a function of density, the parameter remains fairly consistent during the intermediate sintering stage, where the densification rate is greatest.

3. Results and Discussion

Upon sintering, the grain size increases significantly to achieve a lower energy microstructure. The grain size versus temperature plot shown in figure 2 reveals a gradual increase in grain size for the low stability powder throughout the temperature range from 800 to 1400 °C. The moderate and low stability tungsten show reduced grain growth between 1000 and 1200 °C. This is likely a result of Zener pinning from the dispersoid phase, which causes a reduction in grain boundary mobility. The high stability tungsten actually shows a decrease in grain size, which could result from coagulation of the dispersoid phase within the pure tungsten grains.

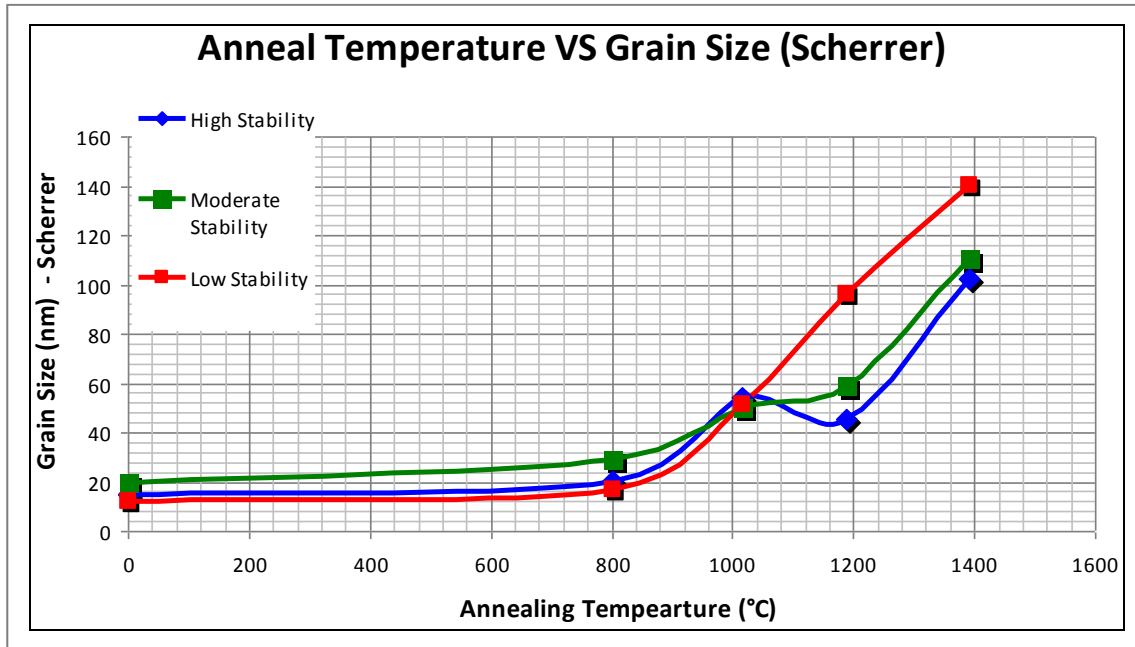


Figure 2. Grain size measurements acquired by x-ray diffraction for each of the thermally stabilized nano-tungsten powders.

Figure 3 shows the microstructures of the three different tungsten powders. While each sample shows a similar density, the grain size of each material indicates that the thermal stability changes significantly based on milling conditions.

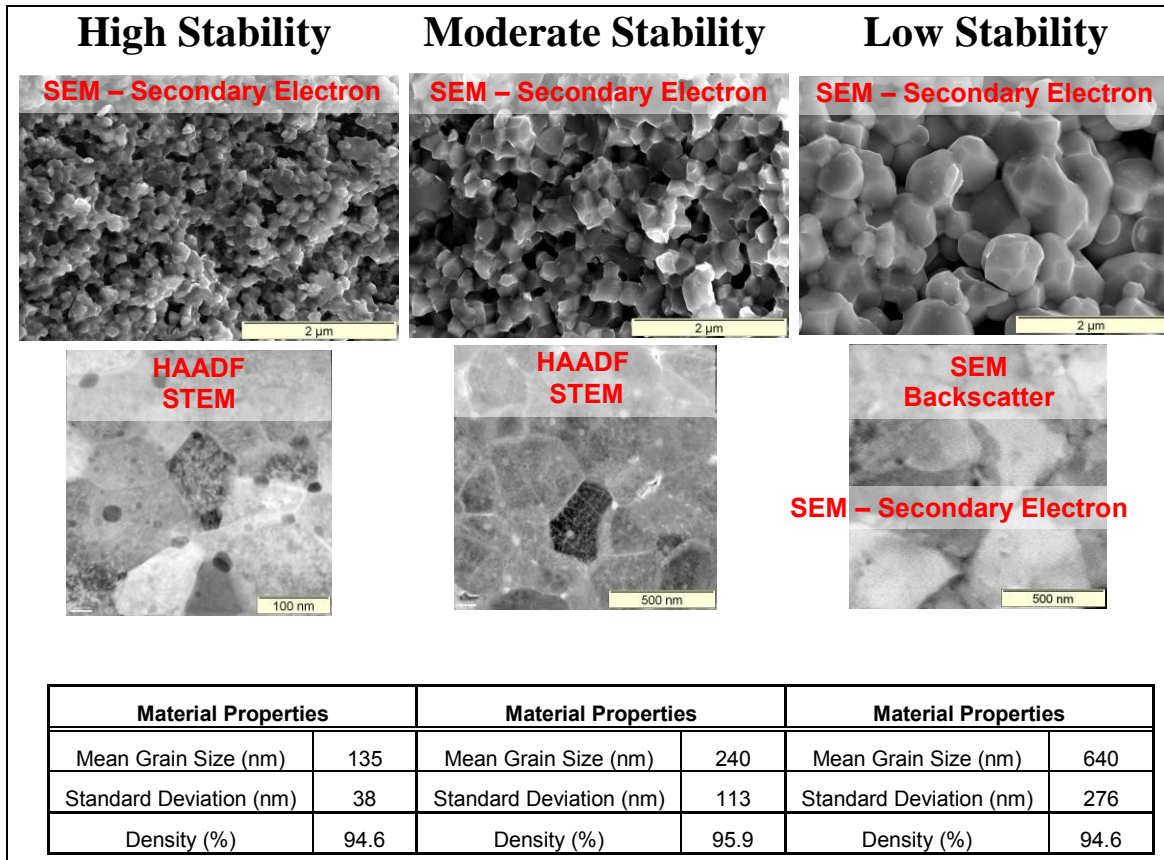


Figure 3. Electron micrographs, grain sizes, and densities of three tungsten samples processed under different milling conditions.

Figure 4 shows the density and densification rate of tungsten as a function of temperature for the HS tungsten sample. These in-situ density measurements were acquired by measuring the linear displacement as a function of temperature at three different heating rates. Similar curves were acquired for the MS and LS samples, though the plots are not shown in this report. Density was calculated assuming isotropic shrinkage, a fair assumption for isostatically pressed compacts.

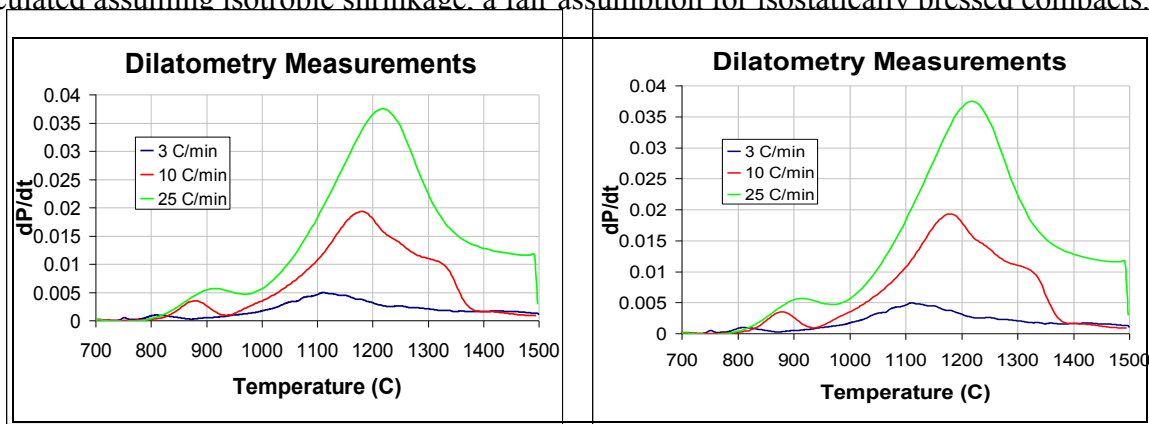


Figure 4. Densification behavior of milled nanostructured tungsten powders.

The density of the tungsten is shown to be a function of both the temperature and the heating rate. The densification rate plot indicates that this is a thermally activated process where the peak shifts with increasing ramp rate. Furthermore, the densification plot shows local maxima at 875–900 °C, indicating a shift in densification mechanisms based upon heating to high temperatures.

The activation energy plotted as a function of density for the HS, MS, and LS samples shows a significant difference in the recorded activation energy corresponding to the degree of thermal stability. The result is shown in figure 5.

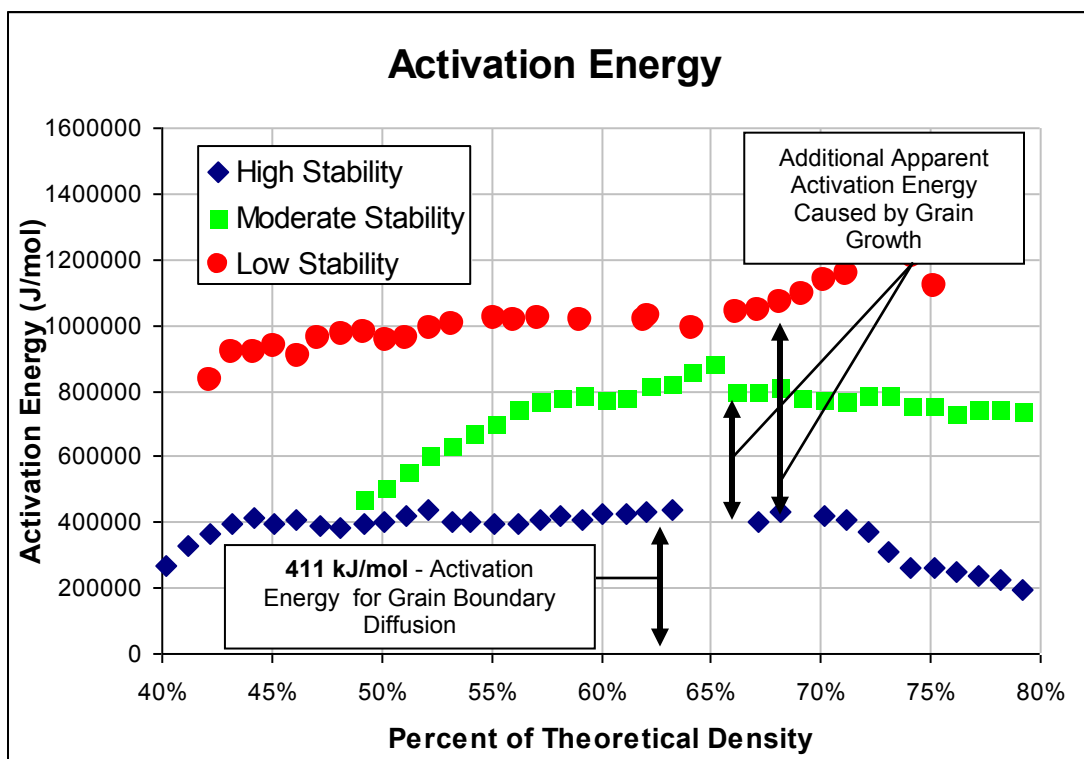


Figure 5. Apparent activation energy for densification of milled tungsten powders exhibiting different degrees of microstructural stability. Note that the differences in initial density are a result of different green packing densities resulting from dissimilar milling conditions.

The activation energy for the highly stable tungsten powder does not fluctuate significantly from the measured activation energy for grain boundary diffusion. The apparent activation energy for densification increases drastically for samples exhibiting moderate to low stability. This increase cannot be described by a different mass transport mechanism operating on the sample as the activation energies are much higher than the standard values listed in table 1. While the implications of the activation energy thermal stability relationship are not immediately apparent from standard chemical kinetics theory, it is important to realize that this number represents the apparent activation energy for densification and not the true activation energy for mass transport to occur. An increase in the apparent activation beyond that for grain boundary diffusion

indicates that a significant portion of the energy is being used to change the structure of the material without contributing to the densification process. Therefore, the deviation from the activation energy for grain boundary diffusion could be correlated to the efficiency of the sintering process for providing a maximum density with minimal energy losses to microstructural changes such as grain growth. While this technique is a very powerful characterization tool, the scope is limited to the temperatures where densification rates are high and can be misleading if a significant amount of coarsening occurs during the final stages of sintering.

Table 1. Measured activation energies for self diffusion based on three mass-transport mechanisms in pure tungsten (20, 28).

Diffusion Type	Activation Energy (kJ/mol)
Surface diffusion	251–287
Grain boundary diffusion	377–460
Volume diffusion	502–586

The average activation energies described by figure 5 show a strong correlation to the grain size measured by electron microscopy. In many cases, the composition can play a vital role in the sintering behavior of materials. The addition of small dispersoids can inhibit the grain growth of a material by effectively reducing the mobility of particle boundaries. It is duly noted that the apparent activation energy for densification is dependent on the concentration of dispersoids in the sample. The relations between composition, activation energy, and the resulting grain size of a sintered sample are shown in figure 6.

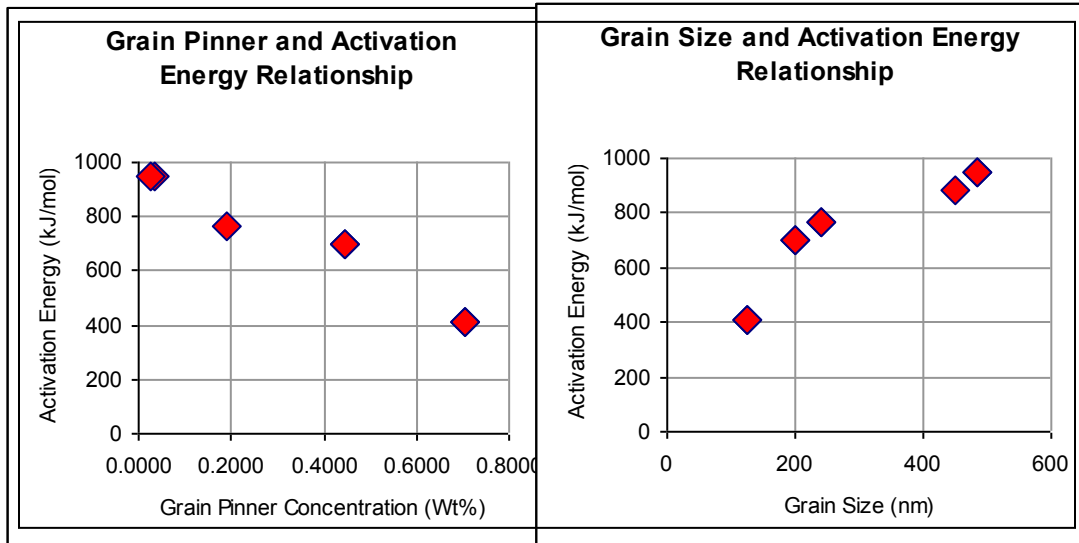
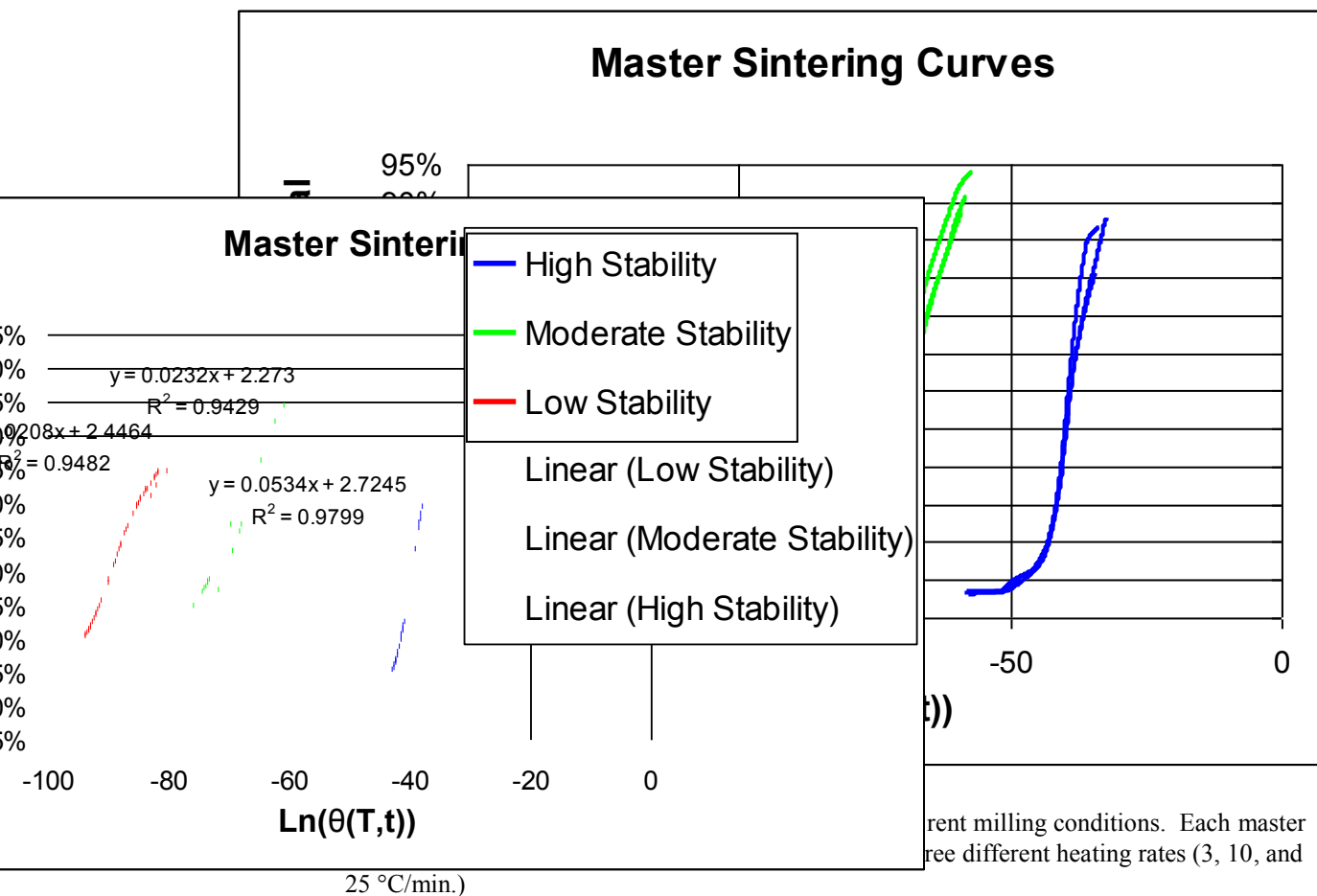


Figure 6. Plot of the measured apparent activation energy as a function of grain pinner concentration and grain size.

The plots in figure 6 demonstrate that the final grain size that results from sintering is dependent on the quantity of grain pinner present in the sample. The measured activation energy is significantly higher than that for grain boundary diffusion for the milled nanocrystalline tungsten with the smallest amount of grain pinner. This deviation describes the instability of the system that results from nanocrystalline grains and high lattice strains. Without any barriers to grain boundary mobility, the energy of the system is relaxed by significant grain growth that occurs independently from the densification process. It is only after the addition of the grain pinning material that the apparent activation energy decreases to the values expected for grain boundary diffusion. These barriers allow the coarsening to occur only in conjunction with densification. This allows for the production of an ideally dense and ultrafine-grained structure. The master sintering curves for the HS, MS, and LS samples are shown in figure 7.



The master sintering curves clearly show that low stability powders can achieve moderate densities with minimal thermal work; however, the slope of the density curve decreases gradually for the LS while the HS material remains fairly constant. This phenomenon is observed as a result of the reduction in the driving force for densification that occurs with grain growth. While the MS sample does show a moderately higher final density compared to the HS and LS samples, this is likely a result of the higher packing density in the green compact.

Similar densities were achieved for samples undergoing the same temperature program in a standard hydrogen furnace. This is a result of the plateau that occurs during the final stages of sintering, where densification is minimal even for a significant amount of thermal energy input.

4. Summary and Conclusions

The thermal stability and densification behavior of a material are critical to producing bulk materials that retain the nanocrystalline properties of the starting powders. Though these parameters are critical to the quality of the final sintered product, they are difficult to measure and are often optimized solely through iterative trial and error experimentation. The use of dilatometry and a combined stage sintering model can help to identify the influence of key processing parameters on the stability and densification behavior of materials. Furthermore, this analysis can identify the optimum thermal stability for minimizing grain growth without inhibiting the diffusion mechanisms that are required for densification. While the master sintering curve is excellent in predicting the sintering curves for a given set of sintering conditions, even minor changes to the powder processing and compaction can have significant influence on the densification parameters and can invalidate the general master sintering curve. Future development of this combined stage sintering model should work to define the influence of initial conditions on the entire sintering process. The resulting model would be an outstanding tool for understanding and predicting the sintering behavior of particulate systems.

5. References

1. Fecht, H. J. et al. Nanocrystalline Metals Prepared by High-energy Ball Milling. *Metallurgical and Materials Transactions A* **1990**, 21 (9), 2333–2337.
2. Brinker, C. J.; Scherer, G. W. *Sol-gel Science: The Physics and Chemistry of Sol-gel Processing*; Academic Press Ltd, 1990.
3. Tong, L.; Reddy, R. G. Synthesis of Titanium Carbide Nano-powders by Thermal Plasma. *Scripta Materialia* **2005**, 52 (12), 1253–1258.
4. Karagedov, G. R.; Lyakhov, N. Z. Preparation and Sintering of Nanosized [alpha]-Al₂O₃ Powder. *Nanostructured Materials* **1999**, 11 (5), 559–572.
5. Siegel, R. W. et al. Synthesis, Characterization and Properties of Nanophase TiO₂. *Journal of Materials Research* **1988**, 3 (6), 1367–1372.
6. Mayo, M. J. Processing of Nanocrystalline Ceramics from Ultrafine Particles. *International Materials Reviews* **1996**, 41 (3), 85–115.
7. Gladman, T. On the Theory of the Effect of Precipitate Particles on Grain Growth in Metals. *Proceedings of the Royal Society of London. Series A, Mathematical and Physical Sciences* **1966**, 294 (1438), 298–309.
8. Cahn, J. W. The Impurity-drag Effect in Grain Boundary Motion. *Acta Metallurgica* **1962**, 10 (9), 789–798.
9. Kirchheim, R. Grain Coarsening Inhibited by Solute Segregation. *Acta Materialia* **2002**, 50 (2), 413–419.
10. VanLeeuwen, B. K. et al. Thermal Stability of Nanocrystalline Pd₈₁Zr₁₉. *Acta Materialia*, in press.
11. Detor, A. J.; Schuh, C. A. Grain Boundary Segregation, Chemical Ordering and Stability of Nanocrystalline Alloys: Atomistic Computer Simulations in the Ni-W System. *Acta Materialia* **2007**, 55 (12), 4221–4232.
12. Shvindlerman, L. S.; Gottstein, G. Efficiency of Drag Mechanisms for Inhibition of Grain Growth in Nanocrystalline Materials. *Zeitschrift für Metallkunde* **2004**, 95 (4), 239–241.
13. Chen, L. C.; Spaepen, F. Analysis of Calorimetric Measurements of Grain Growth. *Journal of Applied Physics* **1991**, 69 (2), 679.
14. Liu, K. W.; Mücklich, F. Thermal Stability of Nano-RuAl Produced by Mechanical Alloying. *Acta Materialia* **2001**, 49 (3), 395–403.

15. Natter, H. et al. Grain-growth Kinetics of Nanocrystalline Iron Studied In Situ by Synchrotron Real-time X-ray Diffraction. *J. Phys. Chem. B* **2000**, *104* (11), 2467–2476.
16. Iordache, M. C. et al. Grain Growth Kinetics in Nanostructured Nickel. *Nanostructured Materials* **1999**, *11* (8), 1343–1349.
17. Moelle, C. H.; Fecht, H. J. Thermal Stability of Nanocrystalline Iron Prepared by Mechanical Attrition. *Nanostructured Materials* **1995**, *6* (1–4), 421–424.
18. Darling, K. A. et al. Grain-size Stabilization in Nanocrystalline FeZr Alloys. *Scripta Materialia* **2008**, *59* (5), 530–533.
19. Perez, R. J.; Huang, B.; Lavernia, E. J. Thermal Stability of Nanocrystalline Fe-10 wt.% Al Produced by Cryogenic Mechanical Alloying. *Nanostructured Materials* **1996**, *7* (5), 565–572.
20. Lassner, E.; Schubert, W. D. *Tungsten: Properties, Chemistry, Technology of the Element, Alloys, and Chemical Compounds*; Kluwer Academic and Plenum Publishers: New York, 1999.
21. German, R. M. *Powder Metallurgy and Particulate Materials Processing*; Metal Powder Industries Federation: Princeton, NJ, 2005, p. 293–294.
22. Su, H.; Johnson, D. L. Master Sintering Curve: A Practical Approach to Sintering. *Journal of the American Ceramic Society* **1996**, *79* (12), 3211–3217.
23. Chen, I. W.; Wang, X. H. Sintering Dense Nanocrystalline Ceramics Without Final-stage Grain Growth. *Nature* **2000**, *404* (6774), 168–171.
24. Gupta, T. K. Possible Correlation Between Density and Grain Size During Sintering. *Journal of the American Ceramic Society* **1972**, *55* (5), 276–277.
25. Rusin, R. P. *Sintering of Nickel Powder With or Without Dispersed Alumina Particles*. Ph.D. Dissertation. Northwestern University, Evanston, IL, June 1993.
26. Wang, J.; Raj, R. Estimate of the Activation Energies for Boundary Diffusion from Rate-controlled Sintering of Pure Alumina, and Alumina Doped with Zirconia or Titania. *Journal of the American Ceramic Society* **1990**, *73* (5), 1172–1175.
27. Kevin, G. E.; Donald, T. E.; Christopher, B. D. Analysis of Nanocrystalline and Microcrystalline ZnO Sintering Using Master Sintering Curves. *Journal of the American Ceramic Society* **2006**, *89* (6), 2003–2009.
28. Bettler, P. C.; Charbonnier, F. M. Activation Energy for the Surface Migration of Tungsten in the Presence of a High-Electric Field. *Physical Review* **1960**, *119* (1), 85.

List of Symbols, Abbreviations, and Acronyms

HS	high stability
LS	low stability
MRD	Materials Research Diffractometer
MS	moderate stability
SEM	scanning electron microscopy
TEM	transmission electron microscopy
XRD	x-ray diffraction

NO. OF
COPIES ORGANIZATION

1
ELEC ADMNSTR
DEFNS TECHL INFO CTR
ATTN DTIC OCP
8725 JOHN J KINGMAN RD STE 0944
FT BELVOIR VA 22060-6218

1 CD OFC OF THE SECY OF DEFNS
ATTN ODDRE (R&AT)
THE PENTAGON
WASHINGTON DC 20301-3080

1 US ARMY RSRCH DEV AND ENGRG
CMND
ARMAMENT RSRCH DEV & ENGRG
CTR
ARMAMENT ENGRG & TECHN LGY
CTR
ATTN AMSRD AAR AEF T J MATTS
BLDG 305
ABERDEEN PROVING GROUND MD
21005-5001

1 PM TIMS, PROFILER (MMS-P)
AN/TMQ-52
ATTN B GRIFFIES
BUILDING 563
FT MONMOUTH NJ 07703

1 US ARMY INFO SYS ENGRG CMND
ATTN AMSEL IE TD A RIVERA
FT HUACHUCA AZ 85613-5300

1 COMMANDER
US ARMY RDECOM
ATTN AMSRD AMR
W C MCCORKLE
5400 FOWLER RD
REDSTONE ARSENAL AL 35898-5000

1 US GOVERNMENT PRINT OFF
DEPOSITORY RECEIVING SECTION
ATTN MAIL STOP IDAD J TATE
732 NORTH CAPITOL ST NW
WASHINGTON DC 20402

3 US ARMY RESEARCH LAB
ATTN RDRL WMM F B BUTLER
ATTN RDRL WMM F H MAUPIN
ATTN RDRL WMM F B KLOTZ
ABERDEEN PROVING GROUND MD
21005

NO. OF
COPIES ORGANIZATION

1 US ARMY RSRCH LAB
ATTN RDRL WMM F E Klier
BLDG 4600
ABERDEEN PROVING GROUND MD
21005

1 US ARMY RSRCH LAB
ATTN RDRL WMM F
M GALLAGHER
ABERDEEN PROVING GROUND MD
21005

1 US ARMY RSRCH LAB
ATTN RDRL CIM G T LANDFRIED
BLDG 4600
ABERDEEN PROVING GROUND MD
21005-5066

3 US ARMY RSRCH LAB
ATTN IMNE ALC HRR
MAIL & RECORDS MGMT
ATTN RDRL CIM L TECHL LIB
ATTN RDRL CIM P TECHL PUB
ADELPHI MD 20783-1197

INTENTIONALLY LEFT BLANK.